Molecular Assembly-Induced Charge Transfer for Programmable Functionalities

As Published: 10.1021/ACS.CHEMMATER.7B04357

Publisher: American Chemical Society (ACS)

Persistent URL: https://hdl.handle.net/1721.1/134331

Version: Author's final manuscript: final author's manuscript post peer review, without publisher's formatting or copy editing

CHEMISTRY OF MATERIALS
Cite This: Chem. Mater. XXXX, XXX, XXX-XXX
Article
pubs.acs.org/cm

Molecular Assembly-Induced Charge Transfer for Programmable Functionalities

Zhuolei Zhang,[†] Huashan Li,[‡,¶] Zhipu Luo,[§] Shuquan Chang,[∥] Zheng Li,[∥] Mengmeng Guan,[⊥] Ziyao Zhou,[⊥] Ming Liu,[⊥] Jeffrey C. Grossman,[‡] and Shenqiang Ren*[,†]

[†]Department of Mechanical Engineering, Temple Materials Institute, Temple University, Philadelphia, Pennsylvania 19122, United States

[‡]Department of Materials Science and Engineering, Massachusetts Institute of Technology, Cambridge, Massachusetts 02139, United States

[§]Synchrotron Radiation Research Section, Macromolecular Crystallography Laboratory, National Cancer Institute, Argonne National Laboratory, Argonne, Illinois 60439, United States

[∥]Jiangsu Engineering Laboratory of Nuclear Energy Equipment Materials, College of Material Science and Technology, Nanjing University of Aeronautics and Astronautics, Nanjing 210016, P. R. China

[⊥]School of Electronic and Information Engineering, Xi'an Jiaotong University, Xi'an, Shaanxi 710049, China

Supporting Information

ABSTRACT: The donor−acceptor interface within molecular charge transfer (CT) solids plays a vital role in the hybridization of molecular orbitals to determine their carrier transport and electronic delocalization. In this study, we demonstrate molecular assembly-driven bilayer and crystalline solids, consisting of electron donor dibenzotetrathiafulvalene (DBTTF) and acceptor C_{60}, in which interfacial engineering-induced CT degree control is a key parameter for tuning its optical, electronic, and magnetic performance. Compared to the DBTTF/C_{60} bilayer structure, the DBTTFC_{60} cocrystalline solids show a stronger degree of charge transfer for broad CT absorption and a large dielectric constant. In addition, the DBTTFC_{60} cocrystals exhibit distinct CT arrangement-driven anisotropic electron mobility and spin characteristics, which further enables the development of high-penetration and high-energy γ-ray photodetectors. The results presented in this paper provide a basis for the design and control of molecular charge transfer solids, which facilitates the integration of such materials into molecular electronics.

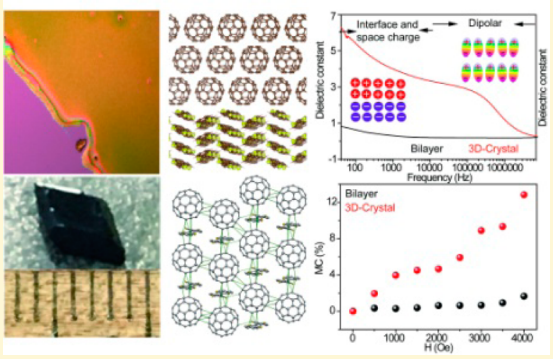

INTRODUCTION

The combination of molecular stacking and electronic variability in van der Waals (vdW)-bonded molecular solids enables the development of a technologically important class of multifunctional molecular artificial materials and emerging devices.[1,2] The hybridization of molecular orbitals across the interfaces permits carrier delocalization and directional charge transfer (CT) interactions, leading to a strong relationship between the molecular packing arrangement and the optical, electrical, magnetic, and transport properties of the CT solids.[3−5] Previous work has shown that distinct molecular CT bilayers can exhibit a range of electronic phases from metallic to superconducting.[6−9] Beyond the CT bilayer materials, three-dimensional (3D) molecular solids can also interact by CT and vdW forces through molecular assembly of donor (D) and acceptor (A) molecular building blocks.[10−13] Such 3D assemblies can possess either mixed or segregated long-range stacking arrangements. The complex molecular precision interface of 3D crystalline CT solids is physically and electronically buried within high-quality crystals, which could lead to emerging device designs and provide new avenues for tuning their physicochemical properties.[14−16] However, despite such promise, the control and manipulation of the density of electronic states of multidimensional CT interfaces remain a crucial bottleneck, limiting the progress of their integration into all-organic solid state devices.

EXPERIMENTAL DETAILS

To form the DBTTF/C_{60} binary materials (hereafter D1), a solution-based processing approach and a further evaporation approach were adopted. The DBTTF materials were dissolved in 1,2-dichlorobenzene (DCB). Because of the low solubility of DBTTF in 1,2-dichlorobenzene at room temperature (~2.6 mg/mL), the temperature of the DBTTF solution was increased to 120 °C and the concentration could be increased to 20 mg/mL. First, the DBTTF solution was spun onto an ITO-patterned glass slide to form a 80 nm thick film at 1500 rpm. The coated devices were heat-treated at 150 °C

Received: October 16, 2017
Revised: October 23, 2017
Published: October 23, 2017

DOI: 10.1021/acs.chemmater.7b04357
Chem. Mater. XXXX, XXX, XXX−XXX

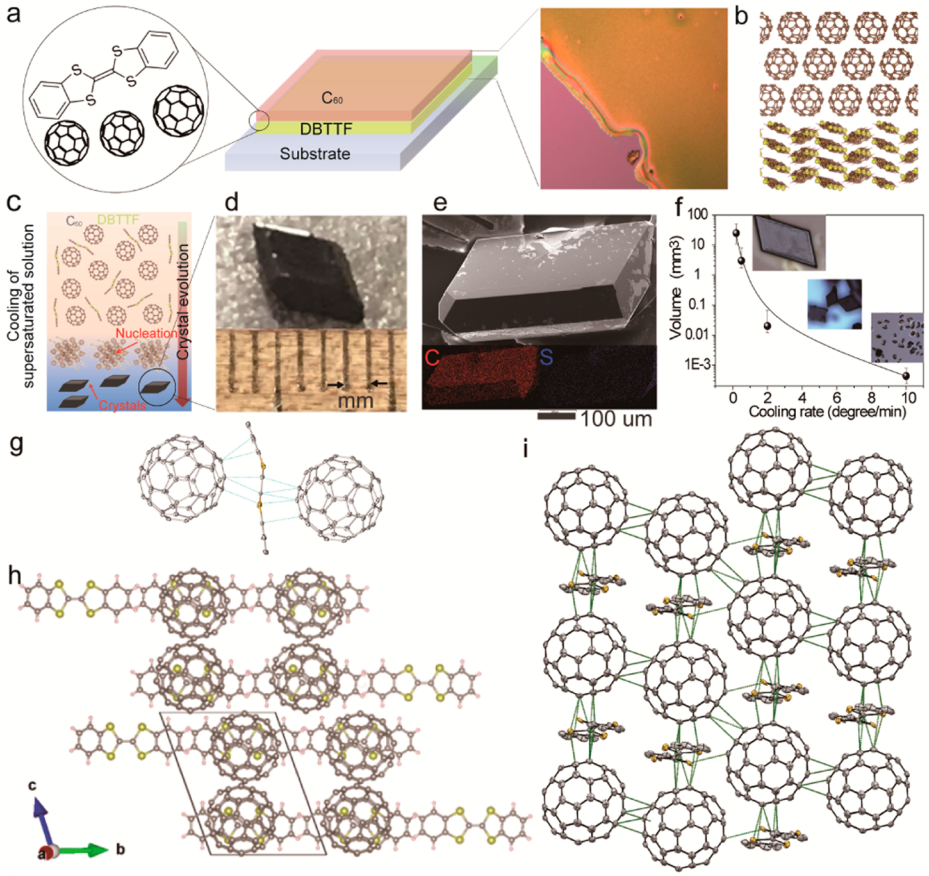

Figure 1. Scheme illustrating the assembly of the D1 and D2 structures and their corresponding morphology and packing arrangements. (a) Assembly of the D1 bilayer structure. The left panel shows the chemical structure of the DBTTF and C_{60} molecule. The middle panel shows the scheme of the D1 bilayer structure. The right panel shows an optical image of the D1 bilayer. (b) Packing arrangement of the D1 bilayer in which DBTTF and C_{60} are crystallized separately and laminated together. (c) Scheme for the growth of the D2 structure by a controlled cooling rate from a supersaturated solution. (d) Photograph of a typical D2 crystal with a volume of ~60 mm^3. (e) SEM image of a D2 crystal, with the bottom showing the elemental mapping. (f) Solution cooling rate-dependent crystal volume. (g) DBTTF conformation and interaction (cyan dashed lines) with C_{60}. (h) Crystal structure of D2 CT along the *a*−*c* plane. (i) Crystal packing of DBTTF and C_{60} and intermolecular contacts (green dashed lines).

for 10 min to increase the crystallinity and then cooled to room temperature; the crystallized DBTTF film could be formed and coated on the substrate continuously. After that, the devices were kept under vacuum (10^{-6} mbar) for >2 h. Then, 80 nm C_{60} and 100 nm Al were evaporated on the top of the DBTTF layer (evaporation rate of ~0.1 nm/s) to act as the active layer and top contact, respectively.

For the assembly of large, high-quality 3D charge transfer crystals (3D-DBTTF/C_{60} crystals, hereafter D2), a method with a controlled cooling rate of a supersaturated solution was applied. DBTTF and C_{60} in a 1:1 mole ratio (the ratio is critical for the synthesis of uniform crystals, as shown in Figure S6) were dissolved in the DCB solvent in a supersaturated state at 120 °C in a nitrogen-filled glovebox and stirred for >48 h to form a homogeneous charge transfer complex. The resulting solution was then cooled to room temperature with various cooling times and further held for certain lengths of time for growth. The cooling rate of the supersaturated solutions significantly influenced the nucleation and crystal growth rate, which is vitally important for tuning the size of D2 crystals. A rapid cooling rate (2 °C/min) resulted in a higher supersaturation level during the cooling period, which would produce more nucleation seeds. The generated nuclei serving as seed crystals depleted the remaining supersaturation during the slow cooling process, resulting in small D2, while a slow cooling rate (0.2 °C/min) caused a lower supersaturation level during the initial cooling period, which induced the generation of fewer nuclei for the large D2 crystals. The pristine single DBTTF and C_{60} crystals were synthesized using the same method as a comparison as shown in Figures S1−S5.

RESULTS AND DISCUSSION

Bilayer Structure and 3D Crystal Structure. In this study, we selected the dibenzotetrathiafulvalene donor (DBTTF, D) (Figures S1−S3) and C_{60} acceptor (A) molecular (Figures S4 and S5) building blocks to investigate the stacking arrangement-driven charge transfer between D and A components within the bilayer and 3D crystal solids. The flat-shaped DBTTF molecule, one of the tetrathiafulvalene derivatives, tends to form low-dimensional arrangements in which π-electron carriers provide a large variety of electronic phases, including charge density waves, spin density waves, and charge localization.[17−19] The fullerene C_{60} is known to be an acceptor that possesses a number of characteristic features, namely, spherical shape, unique electronic structure, high symmetry, and polarizability.[20]

Because of the complex nature of intermolecular interactions within molecular solids, a well-defined interface of molecular solids is desired. In the bilayer geometry, the DBTTF donor and C_{60} acceptor molecules are assembled by a physical evaporation method. For the assembly of 3D crystal solids, the DBTTF donor and C_{60} acceptor molecules are cocrystallized through a supersaturated DBTTF and C_{60} mixed solution for the formation of D2 crystals. (Figure 1c,d and Figures S6−S8). Scanning electron microscopy (SEM) (Figure 1e and Figure

DOI: 10.1021/acs.chemmater.7b04357
Chem. Mater. XXXX, XXX, XXX−XXX

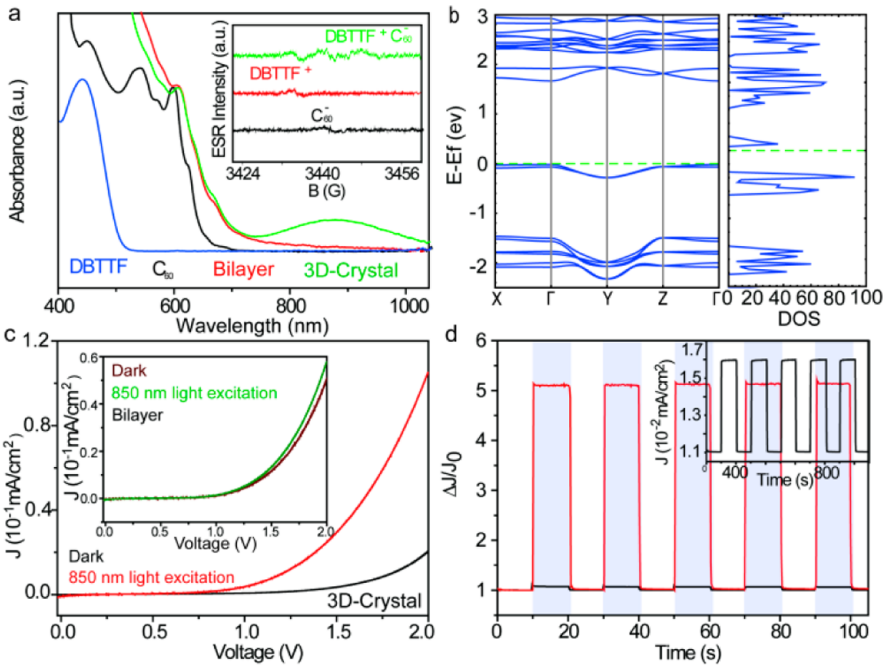

Figure 2. Photoabsorption spectroscopy, calculated electronic structure, and optoelectronic properties of the D1 bilayer and D2 crystal. (a) Photoabsorption spectroscopy of the D1 bilayer and D2 crystal. The inset shows the EPR spectrum of pure DBTTF, C_{60}, and the CT complex. (b) Computed band structure and density of states (DOS) for the D2 crystal, with the Fermi level indicated by the green dashed line. (c) Measured current density−voltage (I−V) curves of the D1 bilayer (inset) and D2 structures in the dark and during 850 nm excitation. (d) Photoresponse of the D1 bilayer and D2 crystal under 850 nm excitation. The inset shows the γ-ray photoresponse of the D2 crystal upon exposure to an excitation of ^{137}Cs source of 0.662 MeV.

S6) reveals a uniform 3D faceted morphology with a homogeneous distribution of carbon and sulfur elements. It should be noted that the cooling rate of the supersaturated solution significantly influences the nucleation and crystal growth to determine the dimension of 3D DBTTFC_{60} crystals (Figure 1f). During a fast cooling process, the nuclei serve as the seed crystals that deplete the remaining supersaturation, resulting in the formation of D2 crystals with an average volume of 0.02 mm^3. In contrast, a slower cooling rate causes a lower supersaturation for the generation of fewer nucleation sites, leading to large D2 crystals with an average volume of 60 mm^3 (4 mm × 5 mm × 3 mm).

Single-crystal X-ray diffraction data of as-grown solids were collected on the SER-CAT 22-ID beamline at the Advance Photon Source of Argonne National Laboratory. The crystal structure of D2 was resolved with in triclinic centrosymmetry space group $P\bar{1}$ (further details in Table S1). From these measurements, we determined that one DBTTF molecule lies between two C_{60} molecules with short intermolecular contacts at S(DBTTF)···C(C_{60}) distances of 3.17−3.44 Å and C-(DBTTF)···C(C_{60}) distances of 3.16−3.37 Å (Figure 1g and Table S2), which are less than the sum of the van der Waals radii of the contact atoms, resulting from the significant intermolecular interaction between DBTTF and C_{60} molecules. The contact distances between C_{60} molecules are in the range of 3.22−3.39 Å (Figure 1h,i and Table S2), and the DBTTF molecular unit is in the *trans* conformation with the cocrystallization of C_{60} (Figure 1g).[21−23]

Electric and Photoelectric Properties of the Bilayer and 3D Crystal Structure. The interplay of significant intermolecular interactions between DBTTF and C_{60} leads to remarkable electronic and charge transfer properties. Changes in the electronic structure upon formation of the D1 bilayer and D2 solids are inferred from photoabsorption spectroscopy (Figure 2a). The broad photoabsorption spectrum of D2 is observed with a distinct band around 900 nm, revealing the strong CT interactions between DBTTF and C_{60} in the 3D crystal structure. By contrast, the D1 bilayer structure shows a narrow absorption. The CT degree and the electronic properties of the geometry-controlled interfacial structures are mainly driven by the molecular orbitals of DBTTF and C_{60} units as well as their specific molecular arrangement.

In addition, from the electron paramagnetic resonance spectrum in the inset of Figure 2a, the pure C_{60} and DBTTF shows a negligible signal while the charge transfer complex shows the C_{60} radical anion and DBTTF radical cation signal. In addition, another resonance peak occurs in the spectrum, which can be attributed to the new splitting peak of the charge transfer excitons. All the new peaks that emerge in the electron paramagnetic resonance spectrum indicate the existence of ground state charge transfer in D2.

This packing-induced CT effect is further illustrated by comparing the band structure and density of states (DOS) of the D2 system (Figure 2b) to those of pristine DBTTF and C_{60} crystals (Figure S9) based on density functional theory (DFT) using the VASP package.[24] A type II energy level alignment is established inside D2, with the HOMO and LUMO wave functions localized at DBTTF and C_{60}, respectively. Moreover, the p states of S atoms in DBTTF molecules comprised the HOMO, while the LUMO is contributed by the p states of C atoms in C_{60} molecules. This infers that charge transfer is occurring between the π^* orbitals of C atoms in C_{60} and the n orbitals of the S atoms in DBTTF.

Because of the broad absorption from the CT interactions, the current density of D2 crystals increases dramatically upon exposure to 850 nm photoexcitation [15.4 mW/cm^2 (Figure

DOI: 10.1021/acs.chemmater.7b04357
Chem. Mater. XXXX, XXX, XXX−XXX

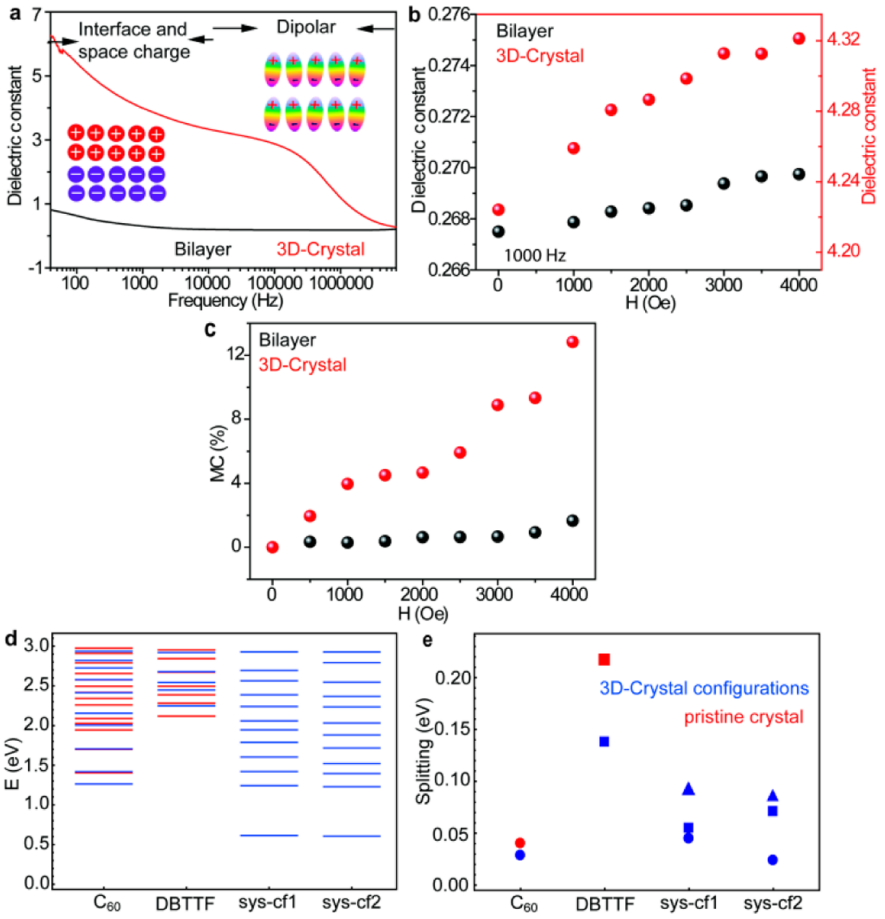

Figure 3. Dipole, magnetic modulation characteristics and time-dependent DFT (TDDFT) simulations of the D1 bilayer and D2 crystal. (a) Frequency-dependent capacitance change of the D1 bilayer and D2 crystal, with space charge and dipole schemes shown. (b) External magnetic field-dependent dielectric constant of the D1 bilayer and D2 crystal. (c) Change in the MC of the D1 bilayer and D2 crystal as a function of a varying magnetic field. (d) Energy levels of singlet excitons and (e) singlet−triplet splitting calculated by TDDFT for isolated C_{60}/DBTTF molecules and pairs of C_{60}/DBTTF molecules in two inequivalent configurations (cf1 and cf2). Red and blue data correspond to the pristine single-crystal and 3D cocrystal configurations, respectively. The circles, squares, and triangles denote data for the excited states dominated by C_{60}, DBTTF, and CT features, respectively.

2c)] in comparison to that of D1 bilayer, confirming a strong degree of charge transfer in 3D crystal solids. Figure 2d shows the photoresponse of the DBTTF/C_{60} bilayer and D2 structures under the 850 nm illumination, where the current density dramatically changes with a repeatable and reversible on/off ratio of ~113% (D1) and 520% (D2). Photoresponses (T) of 0.68 and 5.72 mA/W were obtained for D1 and D2 structures, respectively, which can be calculated with the equation $T = (J_{light} - J_{dark})/L$, where J_{light} and J_{dark} are the current densities under light and dark conditions, respectively, and L is the input light power density.

In addition to the visible-range photoresponse, molecularly densely packed D2 single crystals also exhibit high sensitivity and repeatability under exposure to a high-energy radioactive ^{137}Cs source with a fast photoresponse (inset of Figure 2d). High-penetration γ-ray photons generally demand complete attenuation, efficient carrier generation, and transport for photoactive medium, which enables high-quality 3D DBTTFC_{60} single-crystal solids as an efficient and stable molecular γ-ray photodetector.

Bipolar and Magnetic Modulation Properties of the Bilayer and 3D Crystal Structure. To quantify the magnitude of the charge transfer-induced dipole moment and the extent of polarization,[25−27] the frequency-dependent dielectric constants for the D1 bilayer and D2 solids are shown in Figure 3a. Within the D1 bilayer structure, the DBTTF and C_{60} molecules are packed at the interface with the limited interfacial area and less long-range cooperativity, inducing less dipole formation for a low dielectric constant. In contrast, within the 3D crystal structure, the DBTTF and C_{60} molecules are densely packed in an ordered manner, which is reflected in the magnitude of its dipoles with long-range ordering for a high dielectric constant and capacitance. The space and interfacial polarizations of the D1 bilayer and D2 solids can orient them in the low-frequency range, whereas at a high frequency, the space and interfacial polarizations cannot move instantly; thus, the response is limited, and the dielectric constant can thus be diminished.[28]

Our measurements confirm that the dielectric constant of the D1 bilayer decreases substantially as the frequency increases and almost remains at a small constant value at 10^5 Hz, suggesting that the dielectric constant is contributed by the weak interfacial dipole and space charge polarization. This result is consistent with the bilayer structure in which the electrons and holes are located in the DBTTF and C_{60} layer, respectively, resulting in the weak interfacial polarization. The dielectric constant of the D2 crystal varies over the full

DOI: 10.1021/acs.chemmater.7b04357
Chem. Mater. XXXX, XXX, XXX−XXX

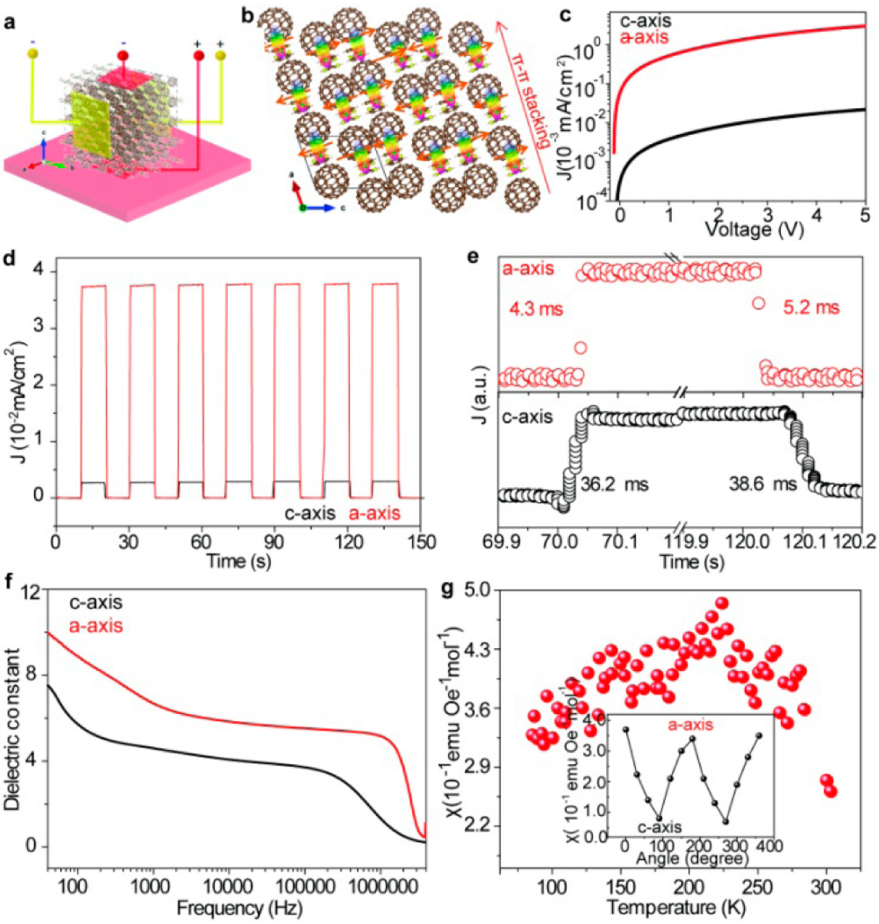

Figure 4. Anisotropic optoelectronics, dipole, and susceptibility of D2 crystals. (a) Illustration of the anisotropy measurement of a single D2 crystal, where the connection between electrodes a and b measures the parallel properties (along the *a*-axis, shown in panel b) and the connection between electrodes a and c or electrodes b and c measures the perpendicular properties (along the *c*-axis, shown in panel b). (b) Molecular packing arrangement along the *a*−*c* plane and the spontaneous long-range ordered dipoles and spin in the 3D D2 crystal, where the ellipse represents the dipole and the orange arrow represents spin. (c) *I*−*V* curve of D2 along the *a*-axis (parallel) and *c*-axis (perpendicular) in the dark. (d and e) Photoresponse of the D2 crystal along the *a*-axis and *c*-axis. (f) Frequency-dependent dielectric constant along the *a*-axis (parallel) and *c*-axis (perpendicular). (g) Temperature-dependent susceptibility change in the D2 crystal, where the inset shows the angle-dependent susceptibility with angles of 0°, 180°, and 360° for the external magnetization parallel to the *a*−*b* plane.

frequency range up to 10^8 Hz, which also exhibits a dielectric constant much higher than that of the D1 bilayer, indicating their more ordered dipole moments and polarization.

While the triplet exciton ordering in the charge transfer structure contributes to the dipole formation and the dielectric constant, an external magnetic field can result in the proportion density change of the triplet exciton due to the competition between spin conservation and spin mixing, leading to a magnetic field-controlled dielectric constant (Figure 3b and Figures S10 and S11). The dielectric constant is increased by 0.69% for the DBTTF/C_{60} bilayer and 1.7% for the D2 crystal under an external magnetic field of 4000 Oe, while the difference is mainly due to the higher density of CT states in the D2 crystal.

Furthermore, because of intersystem crossing in CT states, an external magnetic field provides a unique way to tune and control the electronic transport properties in molecular CT materials, leading to a magneto-conductance effect [MC (Figure 3c and Figures S12 and S13)]. The MC is increased by 1.5% for the D1 bilayer, while a larger 12.8% increase is observed for the 3D DBTTFC_{60} crystal under an external magnetic field of 4000 Oe. Because the external magnetic field induces a conversion from singlet to triplet CT states in the DBTTF/C_{60} bilayer and D2 solids, they can then be partially transferred to polarons and triplet excitons for an increase in the charge density for the positive MC effect.

To further understand the nature of the excited CT states and magnetic field effects in molecular solids, we performed time-dependent DFT (TDDFT) simulations (Tables S3 and S4), as implemented in the Octopus package,[29] for pairs of DBTTF and C_{60} molecules in two inequivalent configurations extracted from the 3D crystal structure. Our results show that the optical gap is 0.61 eV (2.12 eV for isolated DBTTF and 1.40 eV for isolated C_{60}), and a number of CT states emerge over a broad energy range, with their eigenvalues only slightly affected by the interface configuration. Our calculated singlet excitation energies of 1.4, 1.6, 2.0, 2.4, and 2.7 eV (Figure 3d) are in good agreement with experimental data (Figure 2a) and the literature.[30]

We also probed the variation of the singlet−triplet splitting within TDDFT. Our results suggest that the singlet−triplet splitting depends on the nature of the related one-particle state as well as structural deformation. As shown in Figure 3e, the localized excitons within C_{60} provide the smallest singlet−

DOI: 10.1021/acs.chemmater.7b04357
Chem. Mater. XXXX, XXX, XXX−XXX

triplet splitting, which can be explained by the lowest exchange energies originating from unfavorable HOMO−LUMO wave function overlap. The singlet−triplet splitting corresponding to CT excitons within the D2 crystal is smaller than those related to the localized exciton within an isolated DBTTF molecule, but larger than those related to the orbitals derived from DBTTF within the D2 crystal. The large fluctuations obtained in DBTTF-associated exciton states can be decomposed into two factors: bending of an isolated molecule to fit the D2 decreases the splitting by 0.08 eV, while incorporation into the crystal environment contributes another 0.08 eV reduction. On the basis of this analysis, the proportion of triplet excitons in the D2 crystal can be much higher than that in the bilayer structure because of the higher density of CT states and DBTTF deformation, which is consistent with the result that the D2 crystal shows increased modulation of magnetoelectric characteristics, including the magnetic field-controlled dielectric constant and MC effects.

Anisotropy in a Single 3D DBTTFC_{60} Crystal. The long-range ordering in the 3D structure exhibits optical, electric, and magnetic properties that are superior to those of the bilayer. Furthermore, directional bonding and intermolecular interactions within the D2 crystal lead to anisotropic spin and electronic structures induced by molecular packing orientations. The larger overlap of molecular orbitals, richer $\pi-\pi$ stacking interaction, and higher charge density along the in-plane orientation (*a*-axis) facilitate charge transfer as well as the modulation of optoelectronic and magnetoelectric characteristics.

Figure 4a shows the measurement scheme for a D2 single crystal along different orientations. The ordered crystalline networks of electron donors and acceptors result in the formation of spontaneous polarization and simultaneous spin order along the *a*-axis in D2 crystals (Figure 4b). The current density−voltage ($I-V$) curves of the D2 crystal along different orientations are presented in Figure 4c, where the conductivities for the *a*-axis and *c*-axis are 8.7×10^{-10} and 6.8×10^{-12} S/m, respectively. The increased relative conductivity along the *a*-axis results from the unique $\pi-\pi$ stacking arrangement and larger overlap of molecular orbitals, which leads to a larger charge carrier density and mobility.

Figure 4d shows the photoresponse along the two directions under 850 nm light illumination, where the current density dramatically changes with a repeatable and reversible on/off. In addition, the rise and decay time constants can be obtained by fitting the temporal response with the equations $I_{on} = I_0 - A_1 \times \exp[(t - t_0)/\tau_1]$ and $I_{off} = I_0 + A_2 \times \exp[(t - t_2)/\tau_2]$, where I_0 is the dark current, A is a constant, and τ_1 and τ_2 are the rise and decay time constants, respectively.[31] Photoresponse times τ_1 and τ_2 in the perpendicular direction are found to be 36.2 ± 1.6 and 38.6 ± 1.1 ms, respectively, while response times τ_1 and τ_2 of the in-plane device are 4.3 ± 0.4 and 5.2 ± 0.3 ms, respectively (Figure 4e). The faster in-plane photoresponse further suggests a large carrier mobility along the parallel direction (the *a*-axis).

The D2 crystal structure exhibits anisotropic dielectric characteristics along the parallel and perpendicular directions, indicating a more ordered dipole moment and dipole density from the interfacial CT interactions (Figure 4f and Figures S14−S16). Furthermore, the collective formation of excitons in the ordered crystalline D2 networks leads to the formation of simultaneous spin order, as illustrated in Figure 4b. Because of the appreciable long-range spin order, the D2 crystal structure shows antiferromagnetic ordering in the temperature-dependent susceptibility measurement (Figure 4g), which can be explained well by the antiferromagnetic Heisenberg model.[32,33] The negative charge of radical anion $C_{60}^{\bullet}$ is mostly concentrated in the equatorial area of the fullerene acceptor. The long-range magnetic order can be formed upon the transition to synchronized rotation of C_{60} molecules, and therefore, the spins in the fullerene chain along the crystallographic *c*-axis are ordered antiferromagnetically. In addition, the susceptibility exhibits angle-dependent behavior between the in-plane (easy-axis) and out-of-plane (hard-axis) directions (the inset of Figure 4g and Figure S17) because of the spin cone orientation effect, where a narrow spin cone along the stacking axis resulting from the strong charge−lattice coupling promotes spin alignment along the easy axis in D2 solids.

SUMMARY

In conclusion, the degree of interfacial engineering through the molecular assembly facilitates our understanding of the relationship among molecular packing, morphology, and the CT-induced charge−spin ordering and dipole relaxation in molecular functional solids. The interplay between intermolecular interactions enables functionalities that are controlled by external stimuli, as well as charge order-induced spontaneous and hysteretic dipolar and spin ordering of molecular CT solids. The results provide a basis for the design and control of charge transfer in molecular crystals, which is indispensable for the integration of such materials into molecular electronics.

ASSOCIATED CONTENT

Supporting Information

The Supporting Information is available free of charge on the ACS Publications website at DOI: 10.1021/acs.chemmater.7b04357.

Experimental details, including the morphology and chemical analysis of pristine DBTTF, C_{60}, the DBTTF/C_{60} bilayer structure, and 3D DBTTFC_{60} CT crystals and calculated electronic structures determined by DFT; band structure of pristine C_{60}, the DBTTF crystal, and the 3D crystal, including a comparison between energy levels of singlet excitons obtained by TDDFT and experiment for isolated C_{60}, as well as the singlet−triplet splitting in isolated C_{60}, DBTTF molecules, and the 3D crystal; magnetic modulation of the dielectric constant of the DBTTFC_{60} CT complex, including magnetic conductance modulation of the DBTTFC_{60} CT complex; and anisotropic properties of a 3D DBTTFC_{60} crystal induced by molecular packing orientations (PDF)

AUTHOR INFORMATION

Corresponding Author

*E-mail: shenqiang.ren@temple.edu.

ORCID

Shuquan Chang: 0000-0002-2564-2945
Ziyao Zhou: 0000-0002-5484-5442
Ming Liu: 0000-0002-6310-948X
Shenqiang Ren: 0000-0002-9987-3316

Present Address

¶Sino-French Institute of Nuclear Engineering & Technology, Sun Yat-Sen University, Tang-Jia-Wan, Zhuhai City, Guangdong Province, 519-082, PR China.

DOI: 10.1021/acs.chemmater.7b04357
Chem. Mater. XXXX, XXX, XXX−XXX

Author Contributions

Z. Zhang carried out experiments and wrote the paper. H. Li and J. Grossman conducted the theoretical calculation. Z. Luo collected and analyzed the structure information of 3D crystals and bilayer. S. Chang and Z. Li did X-ray detecting experiment. M. Guan, Z. Zhou, and M. Liu performed the EPR experiments. S. Ren leads the project. All authors discussed the results and commented on the manuscript.

Funding

Work at Temple University (S.R.) was supported by the U.S. Department of Energy (DOE), Office of Basic Energy Sciences, Division of Materials Sciences and Engineering, under Grant DE-SC0017928 (organic synthesis and physical property measurement) and the Army Research Office (W911NF-15-1-0610, material design/self-assembly). Work at the Massachusetts Institute of Technology (J.C.G.) was supported by the ExxonMobil Co. This research used resources of the National Energy Research Scientific Computing Center, a DOE Office of Science User Facility supported by the Office of Science of the DOE under Contract DE-AC02-05CH11231. Diffraction data were collected at SER-CAT beamline 22BM at the Advanced Photon Source, Argonne National Laboratory. Use of the Advanced Photon Source was supported by the DOE, Office of Science, Office of Basic Energy Sciences, under Contract W-31-109-Eng-38.

Notes

The authors declare no competing financial interest.

REFERENCES

(1) Brédas, J.-L.; Beljonne, D.; Coropceanu, V.; Cornil, J. Charge-transfer and energy-transfer processes in π-conjugated oligomers and polymers: a molecular picture. *Chem. Rev.* **2004**, *104*, 4971−5004.

(2) Wang, C.; Dong, H.; Hu, W.; Liu, Y.; Zhu, D. Semiconducting π-conjugated systems in field-effect transistors: a material odyssey of organic electronics. *Chem. Rev.* **2012**, *112*, 2208−2267.

(3) Enoki, T.; Miyazaki, A. Magnetic TTF-based charge-transfer complexes. *Chem. Rev.* **2004**, *104*, 5449−5478.

(4) Zhang, Z.; Xu, B.; Xu, B.; Jin, L.; Dai, H. L.; Rao, Y.; Ren, S. External Stimuli Responsive 2D Charge Transfer Polymers. *Adv. Mater. Interfaces* **2017**, *4*, 1600769.

(5) Soos, Z. G. Theory of π-molecular charge-transfer crystals. *Annu. Rev. Phys. Chem.* **1974**, *25*, 121−153.

(6) Alves, H.; Molinari, A. S.; Xie, H.; Morpurgo, A. F. Metallic conduction at organic charge-transfer interfaces. *Nat. Mater.* **2008**, *7*, 574−580.

(7) Abe, T.; Tobinai, S.; Taira, N.; Chiba, J.; Itoh, T.; Nagai, K. Molecular hydrogen evolution by organic p/n bilayer film of phthalocyanine/fullerene in the entire visible-light energy region. *J. Phys. Chem. C* **2011**, *115*, 7701−7705.

(8) Nakano, M.; Alves, H.; Molinari, A. S.; Ono, S.; Minder, N.; Morpurgo, A. F. Small gap semiconducting organic charge-transfer interfaces. *Appl. Phys. Lett.* **2010**, *96*, 232102.

(9) Pron, A.; Rannou, P. Processible conjugated polymers: from organic semiconductors to organic metals and superconductors. *Prog. Polym. Sci.* **2002**, *27*, 135−190.

(10) Xu, B.; Li, H.; Li, H.; Wilson, A. J.; Zhang, L.; Chen, K.; Willets, K. A.; Ren, F.; Grossman, J. C.; Ren, S. Chemically driven interfacial coupling in charge-transfer mediated functional superstructures. *Nano Lett.* **2016**, *16*, 2851−2859.

(11) Zhu, L.; Yi, Y.; Fonari, A.; Corbin, N. S.; Coropceanu, V.; Brédas, J.-L. Electronic Properties of Mixed-Stack Organic Charge-Transfer Crystals. *J. Phys. Chem. C* **2014**, *118*, 14150−14156.

(12) McConnell, H.; Hoffman, B.; Metzger, R. Charge transfer in molecular crystals. *Proc. Natl. Acad. Sci. U. S. A.* **1965**, *53*, 46−50.

(13) Blackburn, A. K.; Sue, A. C.-H.; Shveyd, A. K.; Cao, D.; Tayi, A.; Narayanan, A.; Rolczynski, B. S.; Szarko, J. M.; Bozdemir, O. A.; Wakabayashi, R.; Lehrman, J. A.; Kahr, B.; Chen, L. X.; Nassar, M. S.; Stupp, S. I.; Stoddart, J. F. Lock-Arm Supramolecular Ordering: A Molecular Construction Set for Cocrystallizing Organic Charge Transfer Complexes. *J. Am. Chem. Soc.* **2014**, *136*, 17224−17235.

(14) Zhu, W.; Zheng, R.; Fu, X.; Fu, H.; Shi, Q.; Zhen, Y.; Dong, H.; Hu, W. Revealing the Charge-Transfer Interactions in Self-Assembled Organic Cocrystals: Two-Dimensional Photonic Applications. *Angew. Chem., Int. Ed.* **2015**, *54*, 6785−6789.

(15) Collet, E.; Lemée-Cailleau, M.-H.; Buron-Le Cointe, M.; Cailleau, H.; Wulff, M.; Luty, T.; Koshihara, S.-Y.; Meyer, M.; Toupet, L.; Rabiller, P. Laser-induced ferroelectric structural order in an organic charge-transfer crystal. *Science* **2003**, *300*, 612−615.

(16) Kim, J.; Hubig, S.; Lindeman, S.; Kochi, J. Diels-Alder topochemistry via charge-transfer crystals: novel (thermal) single-crystal-to-single-crystal transformations. *J. Am. Chem. Soc.* **2001**, *123*, 87−95.

(17) Spanget-Larsen, J.; Gleiter, R.; Hünig, S. The electronic structure of dibenzotetrathiafulvalene. *Chem. Phys. Lett.* **1976**, *37*, 29−32.

(18) Nan, G.; Li, Z. Phase dependence of hole mobilities in dibenzotetrathiafulvalene crystal: A first-principles study. *Org. Electron.* **2012**, *13*, 1229−1236.

(19) Emge, T. J.; Wiygul, F. M.; Chappell, J. S.; Bloch, A. N.; Ferraris, J. P.; Cowan, D. O.; Kistenmacher, T. J. Crystal Structures for the Electron Donor Dibenzotetrathiafulavalene, DBTTF, and Its Mixed-stack Charge-transfer Salts with the Electron Acceptors 7, 7, 8, 8-tetracyano-p-quinodimethane, TCNQ, and 2, 5-difluoro-7, 7, 8, 8-tetracyano-p-quinodimethane, 2, 5-TCNQF_2. *Mol. Cryst. Liq. Cryst.* **1982**, *87*, 137−161.

(20) Konarev, D. V.; Lyubovskaya, R. N.; Drichko, N. V.; Yudanova, E. I.; Shul'ga, Y. M.; Litvinov, A. L.; Semkin, V. N.; Tarasov, B. P. Donor−acceptor complexes of fullerene C_{60} with organic and organometallic donors. *J. Mater. Chem.* **2000**, *10*, 803−818.

(21) Mamada, M.; Yamashita, Y. Triclinic polymorph of dibenzotetrathiafulvalene. *Acta Crystallogr., Sect. E: Struct. Rep. Online* **2009**, *65*, o2083−o2083.

(22) Konarev, D.; Zubavichus, Y.; Slovokhotov, Y. L.; Shul'ga, Y. M.; Semkin, V.; Drichko, N.; Lyubovskaya, R. New complexes of fullerenes C_{60} and C_{70} with organic donor DBTTF: synthesis, some properties and crystal structure of DBTTF· C_{60}· C_6H_6 (DBTTF= dibenzotetrathiafulvalene). *Synth. Met.* **1998**, *92*, 1−6.

(23) Knight, B. W.; Purrington, S. T.; Bereman, R. D.; Singh, P. A new tetrathiafulvalene derivative containing fluorine attached to the π-system. *Synthesis* **1994**, *1994*, 460−462.

(24) Kresse, G.; Furthmüller, J. Efficiency of ab-initio total energy calculations for metals and semiconductors using a plane-wave basis set. *Comput. Mater. Sci.* **1996**, *6*, 15−50.

(25) Goetz, K. P.; Vermeulen, D.; Payne, M. E.; Kloc, C.; McNeil, L. E.; Jurchescu, O. D. Charge-transfer complexes: new perspectives on an old class of compounds. *J. Mater. Chem. C* **2014**, *2*, 3065−3076.

(26) Baldo, M. A.; O'brien, D.; You, Y.; Shoustikov, A.; Sibley, S.; Thompson, M.; Forrest, S. Highly efficient phosphorescent emission from organic electroluminescent devices. *Nature* **1998**, *395*, 151−154.

(27) Jariwala, D.; Sangwan, V. K.; Lauhon, L. J.; Marks, T. J.; Hersam, M. C. Carbon nanomaterials for electronics, optoelectronics, photovoltaics, and sensing. *Chem. Soc. Rev.* **2013**, *42*, 2824−2860.

(28) Alias, R. *Structural and Dielectric Properties of Glass-Ceramic Substrate with Varied Sintering Temperatures*; InTech: Rijeka, Croatia, 2013.

(29) Andrade, X.; Strubbe, D.; De Giovannini, U.; Larsen, A. H.; Oliveira, M. J.; Alberdi-Rodriguez, J.; Varas, A.; Theophilou, I.; Helbig, N.; Verstraete, M. J.; Stella, L.; Nogueira, F.; Aspuru-Guzik, A.; Castro, A.; Marques, M. A. L.; Rubio, A. Real-space grids and the Octopus code as tools for the development of new simulation approaches for electronic systems. *Phys. Chem. Chem. Phys.* **2015**, *17*, 31371−31396.

(30) Ebbesen, T. W.; Tanigaki, K.; Kuroshima, S. Excited-state properties of C_{60}. *Chem. Phys. Lett.* **1991**, *181*, 501−504.

DOI: 10.1021/acs.chemmater.7b04357
Chem. Mater. XXXX, XXX, XXX−XXX

(31) Zhang, Z.; Xu, B.; Zhang, L.; Ren, S. Hybrid chalcopyrite−polymer magnetoconducting materials. *ACS Appl. Mater. Interfaces* **2016**, *8*, 11215−11220.
(32) Deplano, P.; Leoni, L.; Laura Mercuri, M.; Schlueter, J. A.; Geiser, U.; Wang, H. H.; Kini, A. M.; Manson, J. L.; Gómez-García, C. J.; Coronado, E.; Koo, H.-J.; Whangbo, M.-H. A two-dimensional radical salt based upon BEDT-TTF and the dimeric, magnetic anion [Fe (tdas) $_2$] 2 2−:(BEDT-TTF)$_2$ [Fe (tdas)$_2$](tdas= 1, 2, 5-thiadiazole-3, 4-dithiolate). *J. Mater. Chem.* **2002**, *12*, 3570−3577.
(33) Clement, R.; Girerd, J.; Morgenstern-Badarau, I. Dramatic modification of the magnetic properties of lamellar manganese trithiophosphonite (MnPS3) upon intercalation. *Inorg. Chem.* **1980**, *19*, 2852−2854.

DOI: 10.1021/acs.chemmater.7b04357
Chem. Mater. XXXX, XXX, XXX−XXX